

# Whole device gyrokinetic simulations using unstructured meshes in realistic tokamak geometry

Z.X. Lu,<sup>1</sup> Ph. Lauber,<sup>1</sup> T. Hayward-Schneider,<sup>1</sup> A. Bottino,<sup>1</sup> and M. Hoelzl<sup>1</sup>  
*Max-Planck-Institut für Plasmaphysik, 85748 Garching, Germany*

(Dated: August 8th, 2019)

In this work, we have formulated and implemented the mixed unstructured mesh based finite element Fourier spectrum scheme for gyrokinetic simulation in realistic tokamak geometry. An efficient particle deposition scheme using an intermediate grid as the search index for triangles has been implemented and a significant speed-up by a factor of  $\sim 30$  is observed as compared with the brute force scheme for a medium size simulation. The TRIMEG (TRIangular MESH based Gyrokinetic) code has been developed. As an application, the ion temperature gradient (ITG) mode is simulated using the simplified gyrokinetic-Poisson model. Our simulation and that using ORB5 code for the DIII-D Cyclone case shows reasonable agreement. As an additional application, ITG simulations using an ASDEX Upgrade equilibrium have been performed with density and temperature gradient profiles similar to the Cyclone case. Capabilities of the TRIMEG code for the realistic experiment equilibrium in the plasma core and in the whole plasma volume with the open field line are demonstrated.

## I. INTRODUCTION

Gyrokinetic simulations play an important role in predicting the transport level due to neoclassical physics or turbulence<sup>1-7</sup>. One of the leading methods is the particle-in-cell (PIC) method. Numerous PIC codes, such as GTC<sup>2</sup>, GEM<sup>8</sup>, ORB5<sup>9</sup>, have been developed for simulations in the core of the tokamak plasmas. Edge plasma simulations have attracted significant attention in recent years due to its connection to the high confinement regime of tokamak plasmas, the prediction of the divertor heat-flux width of ITER<sup>10</sup>, edge localized mode (ELM) control<sup>11</sup> etc. In order to simulate the edge physics, besides the comprehensive physics model<sup>12,13</sup>, numerical schemes such as finite element methods for unstructured meshes in XGC<sup>5,14</sup>, GTS<sup>4</sup> and GTC/GTC-X<sup>15,16</sup> and multiple patches of structured meshes in JOREK<sup>11</sup> have been developed in order to treat the open field line (OFL) region. While whole device simulations for neoclassical transport, ELMs and micro-turbulence have been reported and various numerical schemes have been developed for treating the OFL geometry and particle deposition to grids<sup>5,10,11,15,17,18</sup>, there is still space to understand the features of different schemes, such as the particle-in-Fourier method<sup>19,20</sup>, and thus to optimize the efficiency and the fidelity of the whole volume simulation.

In this work, we developed the mixed unstructured mesh based finite element Fourier decomposition scheme, i.e., the mixed particle-in-cell-particle-in-Fourier (PIC-PIF) scheme, for the gyrokinetic simulation in general tokamak geometry, with the OFL region included. In addition, an efficient particle deposition scheme using an intermediate grid as the search index for triangles has been implemented. This work is organized as follows. In Section II, the physics model and numerical schemes are given. In Section III, we perform the convergence/scaling studies and the simulation of ion temperature gradient (ITG) mode using the DIII-D cyclone parameters and the AUG realistic equilibrium. In IV, the conclusions

and outlook are given.

## II. PHYSICS MODEL AND NUMERICAL METHODS

In the following, we will define the normalization in Section II A. In Sections II B–II D, we will describe the three basic classes in the code, namely, the equilibrium, the particle and the field classes. On the other hand, we will also describe the numerical methods in Section II E. The details related to the finite element and unstructured meshes are described in our previous work for circular tokamak geometry<sup>21</sup> and will be omitted in this work.

### A. Normalization

Normalization units are defined and physics quantities are normalized to the normalization units. The length unit is  $R_N = 1m$ . The velocity unit is  $v_N = v_{th,hy}$ , where  $v_{th,hy} = \sqrt{2T_h/m_{hy}}$ ,  $T_{hy}$  is the reference temperature,  $m_{hy}$  is the mass of hydrogen, the subscripts ‘N’ and ‘hy’ indicate “normalization” and “hydrogen” respectively. For each particle species,  $v_{th,s}$  is used when markers are loaded while unit conversion to the normalization unit is performed in the particles’ equations of motion and the field equation. The time unit is  $R_N/v_{th,hy}$ . The magnetic field unit is  $B_N = 1T$ .

### B. The coordinates and the equilibrium

In the right-handed coordinates  $(R, \varphi, Z)$  and  $(\psi, \varphi, \theta)$ , using EFIT convention, the magnetic field is represented as

$$\mathbf{B} = \nabla\psi \times \nabla\varphi + F\nabla\varphi . \quad (1)$$

In the  $(\psi, \varphi, \theta)$  coordinates, the safety factor is defined as  $q = \mathbf{B} \cdot \nabla\varphi / (\mathbf{B} \cdot \nabla\theta) = JF/R^2$ , where  $J = \{\nabla\psi \times \nabla\varphi \cdot$

$\nabla\theta\}^{-1}$ . The equilibrium variables are constructed using B-spline in  $(R, Z)$  plane of the  $(R, \varphi, Z)$  coordinates. The equilibrium variables such as  $B$ ,  $B_R$  and  $B_Z$  can be obtained using the B-spline subroutines.

The hybrid coordinates  $(R, \varphi, Z)$  and  $(\psi, \varphi, \theta)$  are used. On one hand, the user specified computation grids are aligned along the magnetic flux surface using the  $\psi$  coordinate, or, if the OFL region is included, along the plasma boundary; the refinement grids are generated when the Delaunay refinement algorithms is called for the generation of the unstructured meshes<sup>22</sup>. The refinement grids using the Delaunay algorithm are not necessarily along the magnetic flux surface but it is a widely used technique for the improvement of the mesh quality. Two cases of the grids and the unstructured meshes for the simulation in Section III are shown in Fig. 1. More details about the finite element for the unstructured meshes are reported in our previous work<sup>21</sup>. On the other hand, in order to treat the open field line geometry, the equations for the field and particles are solved in  $(R, \varphi, Z)$  coordinates. The magnetic field is expressed as

$$B_R = -\frac{1}{R} \frac{\partial \psi}{\partial Z}, \quad B_Z = +\frac{1}{R} \frac{\partial \psi}{\partial R}, \quad B_\varphi = F/R. \quad (2)$$

The parallel derivative is

$$\partial_{\parallel} \delta \phi = \left( b_R \partial_R + b_Z \partial_Z + \frac{b_\phi}{R} \partial_\phi \right) \delta \phi, \quad (3)$$

where  $\delta \phi$  is the perturbed electrostatic scalar potential,  $b_R = B_R/B$ ,  $b_Z = B_Z/B$  and  $b_\phi = B_\phi/B$ .

The field-aligned coordinates are constructed for parallel derivatives. Along the magnetic field line  $\mathbf{B}$ , the auxiliary Clebsch coordinates  $(\chi, \xi, l)$  are determined by

$$\left. \frac{dR(\chi, \xi, l)}{d\phi} \right|_{\chi, \xi} = R \frac{B_R}{B_\phi}, \quad (4)$$

$$\left. \frac{dZ(\chi, \xi, l)}{d\phi} \right|_{\chi, \xi} = R \frac{B_Z}{B_\phi}, \quad (5)$$

$$\left. \frac{dl}{d\phi} \right|_{\chi, \xi} = R \frac{B}{B_\phi}, \quad (6)$$

where  $(\chi, \xi)$  labels a magnetic field and  $l$  is the coordinate along  $\mathbf{B}$ . The parallel derivative using these Clebsch coordinates is

$$\partial_{\parallel} \delta \phi = \left. \frac{\partial}{\partial l} \right|_{\chi, \xi} \delta \phi. \quad (7)$$

For parallel derivatives of high  $n$  (toroidal mode number) field aligned modes, Eq. 7 can provide high accuracy compared with Eq. 3.

## C. Particles

### 1. Equations of motion

In this work, we focus on electrostatic simulations. In order to describe the particle guiding center motion,

we follow the canonical Hamiltonian equations<sup>23</sup>. Using  $(\mathbf{R}, \rho_{\parallel}, \mu)$  as the guiding center coordinates, the equations of motion are as follows,

$$\dot{\mathbf{R}} = \frac{1}{e\mathbf{B} \cdot \mathbf{B}_{\parallel}^*} \left[ \frac{e^2 B^2 \rho_{\parallel}}{m} \mathbf{B}_{\parallel}^* + \mathbf{B} \times \nabla H \right], \quad (8)$$

$$\dot{\rho}_{\parallel} = -\frac{1}{e\mathbf{B} \cdot \mathbf{B}_{\parallel}^*} \left( \mathbf{B}_{\parallel}^* \cdot \nabla H \right), \quad (9)$$

where  $\mathbf{B}_{\parallel}^* = \mathbf{B} + \rho_{\parallel} \nabla \times \mathbf{B}$ ,  $\rho_{\parallel} = mv_{\parallel}/(ZeB)$ ,  $Z$  is the charge number,  $H = e^2 \rho_{\parallel}^2 B^2 / (2mc^2) + m\mu B + e\delta\phi$  is the Hamiltonian, and  $\mu = v_{\perp}^2 / (2B)$ . The equations of motion above are equivalent to those adopted in XGC<sup>5</sup>,

$$\dot{\mathbf{x}} = (1/D)[v_{\parallel} \mathbf{b} + v_{\parallel}^2 \nabla B \times \mathbf{b} + B \times (\mu \nabla B - E)/B^2] \quad (10)$$

$$\dot{v}_{\parallel} = -(1/D)(B + v_{\parallel} \nabla B \times \mathbf{b}) \cdot (\mu \nabla B - E), \quad (11)$$

where  $D \equiv 1 + v_{\parallel} \mathbf{b} \cdot \nabla \times \mathbf{b}/B$  is related to the higher order corrections.

The variables  $\dot{\mathbf{R}}, \dot{v}_{\parallel}$  can be written as

$$\dot{\mathbf{R}} = \mathbf{v}_{\parallel 0} + \mathbf{v}_{d0} + \mathbf{v}_E, \quad (12)$$

$$\dot{v}_{\parallel} = \dot{v}_{\parallel 0} + \dot{v}_{\parallel E}, \quad (13)$$

where the subscript 0 and  $E$  indicate the particle motion in equilibrium and that due to the electrostatic field. In  $(R, \varphi, Z)$  coordinates, the contravariant components of the velocity  $v^\alpha \equiv \mathbf{v} \cdot \nabla \alpha$  are calculated for different terms.

#### 1. Magnetic drift $\mathbf{v}_{d0}$

$$v_{d0}^R = \frac{v_{\parallel}^2 + v_{\perp}^2/2}{\omega_c} \frac{b_\varphi}{RB_{\parallel}^*} \partial_Z B, \quad (14)$$

$$v_{d0}^Z = -\frac{v_{\parallel}^2 + v_{\perp}^2/2}{\omega_c} \frac{b_\varphi}{RB_{\parallel}^*} \partial_R B, \quad (15)$$

$$v_{d0}^\varphi = \frac{v_{\parallel}^2 + v_{\perp}^2/2}{\omega_c} \frac{1}{RB_{\parallel}^*} (-b_R \partial_Z B + b_Z \partial_R B). \quad (16)$$

The dominant terms of the equations of motion are obtained by omitting the terms of order of  $\rho^* = \rho_{th}/a$  and of  $B_\theta/B$ , where  $\rho_{th} = mv_{th}/(ZeB)$ ,  $v_{th} = \sqrt{2T/m}$ . In  $(R, \varphi, Z)$  coordinates, the dominant terms in the equations of motion are

$$\mathbf{v}_{d0} \approx \frac{v_{\perp}^2 + 2v_{\parallel}^2}{2\omega_c} \mathbf{b} \times \nabla B,$$

which, noticing that  $\mathbf{b} \approx b_\phi \hat{\phi}$ , where  $\hat{\phi}$  is the unit vector in the toroidal direction, and  $B \approx B_\phi$ , can be further reduced to,

$$v_{d0}^R \approx 0, \quad v_{d0}^Z \approx -b_\phi \frac{v_{\parallel}^2 + v_{\perp}^2/2}{\omega_c} \partial_R B_\phi. \quad (17)$$

## 2. $E \times B$ drift $\mathbf{v}_E$

$$\delta v_E^R = \frac{1}{B_{\parallel}^*} (b_{\varphi} \partial_Z \langle \delta \phi \rangle - \frac{b_Z}{R} \partial_{\varphi} \langle \delta \phi \rangle) , \quad (18)$$

$$\delta v_E^Z = \frac{1}{B_{\parallel}^*} (-b_{\varphi} \partial_R \langle \delta \phi \rangle + \frac{b_R}{R} \partial_{\varphi} \langle \delta \phi \rangle) , \quad (19)$$

$$\delta v_E^{\varphi} = \frac{1}{RB_{\parallel}^*} (-b_R \partial_Z \langle \delta \phi \rangle + b_Z \partial_R \langle \delta \phi \rangle) , \quad (20)$$

where  $\langle \dots \rangle$  indicates the gyro average. The dominant term is

$$\delta \mathbf{v}_{E \times B} = \mathbf{b} \times \nabla \delta \varphi / B = \frac{1}{B} [\hat{R} \partial_Z \delta \varphi - \hat{Z} \partial_R \delta \varphi] \quad (21)$$

where  $\hat{R}$  and  $\hat{Z}$  are the unit vectors in the  $R$  and  $Z$  directions.

## 3. Parallel acceleration $\dot{v}_{\parallel 0}$

$$\dot{v}_{\parallel 0} = -\frac{\mu}{B_{\parallel}^*} (B_R^* \partial_R B + B_Z^* \partial_Z B). \quad (22)$$

The dominant term is

$$\dot{v}_{\parallel 0} \approx -\mu (b_R \partial_R B + b_Z \partial_Z B). \quad (23)$$

The simplification of other terms such as  $v_{\parallel}$  and  $\dot{v}_{\parallel E}$  is trivial and is omitted.

## 2. Weight equation

The equation for the evolution of the perturbed distribution function  $\delta f(\mathbf{R}, v_{\parallel})$  is

$$\frac{d\delta f}{dt} = \tau(\mathbf{E}) , \quad (24)$$

where

$$\tau(\mathbf{E}) = -f_0 \delta \mathbf{R} \cdot \nabla \ln f_0 + f_0 \frac{e}{m} \langle \mathbf{E} \rangle \cdot \frac{d\mathbf{R}}{dt} \Big|_0 .$$

The weight of the markers is defined to represent the perturbed distribution function,

$$\begin{aligned} \delta f(\mathbf{R}, v_{\parallel}, \mu) &= \frac{N_{ph}}{N} \sum_{p=1}^N \frac{1}{2\pi B_{\parallel}^*} w_p(t) \delta(\mathbf{R} - \mathbf{R}_p(t)) \\ &\quad \times \delta(v_{\parallel} - v_{\parallel,p}(t)) \delta(\mu - \mu_p(t)) , \end{aligned} \quad (25)$$

where  $N_{ph}$  and  $N$  are the total physical particle number and marker number and the subscript  $p$  is the marker index. Defining  $\Omega_p$  as the phase space volume occupied by the marker  $p$ , Eq. 25 yields

$$\delta f(\mathbf{R}_p, v_{\parallel,p}, \mu_p) \Omega_p = \frac{N_{ph}}{N} w_p(t) , \quad (26)$$

and Eq. 24 gives

$$\frac{dw_p}{dt} = \frac{N}{N_{ph}} \Omega_p \tau(\mathbf{E}) . \quad (27)$$

The above definition is the same as that in ORB5<sup>9,24</sup>. However, in this work, for the sake of simplicity, we load the markers with the distribution function the same as the physical particles, i.e.,

$$f_{\text{mark}} = \frac{N}{N_{ph}} f , \quad (28)$$

then

$$\Omega_p \equiv \frac{B_{\parallel}^* d\mathbf{R} d\mu d\alpha}{dN} = \frac{1}{f_{\text{mark}}} , \quad (29)$$

where  $\alpha$  is the gyro angle. Equations 27, 28 and 29 yield

$$\frac{dw}{dt} = -\delta \mathbf{R} \cdot \nabla \ln f_0 + \frac{e}{m} \langle \mathbf{E} \rangle \cdot \frac{d\mathbf{R}}{dt} \Big|_0 . \quad (30)$$

The perturbed density in a small volume  $\Delta V$  is calculated from the marker weight in  $\Delta V$

$$\frac{\delta n}{\langle n \rangle} = \frac{V_{\text{tot}}}{N \Delta V} \sum_{p \in \Delta V} w_p , \quad (31)$$

where  $\langle n \rangle$  is the volume averaged density. For unstructured meshes, the volume  $\Delta V$  is centered with a vertex and  $\Delta V = \Delta V_{\text{vert}}$  is calculated using  $\Delta V_{\text{tria}}$ , where  $\Delta V_{\text{tria}}$  is a triangular prism which extends along the  $\varphi$  direction. Using particle-in-Fourier in toroidal direction, we have for each toroidal mode number  $n$ ,

$$\frac{\delta n_n(R, Z)}{\langle n \rangle} = \frac{V_{\text{tot}}}{N \Delta V} \sum_{(R_p, Z_p) \in \Delta S} w_p e^{-in\varphi_p} , \quad (32)$$

where  $\Delta S$  is the projection of  $\Delta V$  in the  $(R, Z)$  plane.

## D. Field equation

The Poisson equation with the long wavelength approximation is adopted in this work, i.e.,

$$-\nabla_{\perp} \frac{n_0}{\omega_c B} \cdot \nabla_{\perp} \delta \phi = \delta n_i - \delta n_e . \quad (33)$$

Generally, the electron response is dominated by the adiabatic response. Thus, the electron response can be decomposed into the adiabatic and non adiabatic (NA) parts, i.e.,

$$\delta n_e = \frac{e}{T_e} \delta \tilde{\phi} + \delta n_e^{NA} , \quad (34)$$

where  $\delta \tilde{\phi}$  is the non-zonal component, i.e.,  $\delta \tilde{\phi} = \delta \phi - \delta \phi_{0,0}$ ,  $\delta \phi_{0,0}$  is the poloidal component with  $n = 0, m = 0$ , where  $m$  is the poloidal mode number. Notice that

Fourier decomposition is used in the  $\phi$  direction but the finite element method is used in  $(R, Z)$  direction.

For  $n \neq 0$ ,

$$-\nabla_{\perp} \frac{n_0}{\omega_c B} \cdot \nabla_{\perp} \delta\phi + \frac{e}{T_e} \delta\tilde{\phi} = \delta n_i - \delta n_e^{NA} . \quad (35)$$

For  $n = 0$ ,

$$-\nabla_{\perp} \frac{n_0}{\omega_c B} \cdot \nabla_{\perp} \delta\phi + \frac{e}{T_e} (\delta\tilde{\phi} - \delta\phi_{0,0}) = \delta n_i - \delta n_e^{NA} . \quad (36)$$

In this work, we focus on the  $n \neq 0$  modes while the studies involving  $n = 0$  components such as the geodesic acoustic mode will be reported in another separate work<sup>21</sup>.

## E. Numerical methods

### 1. General description

This gyrokinetic-Poisson system is implemented in Fortran. The field equation is solved using finite element methods for unstructured meshes. The sparse matrix corresponding to the Poisson equation is solved using PETSc (Portable, Extensible Toolkit for Scientific Computation)<sup>25</sup>. The Runge-Kutta fourth order integrator is implemented for particles and coupled to the field solver. The RungeKutta fourth-order method is given by the following steps,

$$\begin{aligned} \Delta\mathbf{X}_1 &= \Delta t d_t \mathbf{X}(\mathbf{X}_t, \delta\phi_t) , & \mathbf{X}_t^{(1)} &= \mathbf{X}_t + \Delta\mathbf{X}_1/2 \\ \Delta\mathbf{X}_2 &= \Delta t d_t \mathbf{X}(\mathbf{X}_t^{(1)}, \delta\phi_t^{(1)}) , & \mathbf{X}_t^{(2)} &= \mathbf{X}_t + \Delta\mathbf{X}_2/2 \\ \Delta\mathbf{X}_3 &= \Delta t d_t \mathbf{X}(\mathbf{X}_t^{(2)}, \delta\phi_t^{(2)}) , & \mathbf{X}_t^{(3)} &= \mathbf{X}_t + \Delta\mathbf{X}_3/2 \\ \Delta\mathbf{X}_4 &= \Delta t d_t \mathbf{X}(\mathbf{X}_t^{(3)}, \delta\phi_t^{(3)}) , \\ \mathbf{X}(t + \Delta t) &= \mathbf{X}(t) + (\Delta\mathbf{X}_1 + 2\Delta\mathbf{X}_2 + 2\Delta\mathbf{X}_3 + \Delta\mathbf{X}_4)/6 , \end{aligned}$$

where  $d_t \mathbf{X} = d\mathbf{X}/dt$ ,  $\mathbf{X} = (\mathbf{R}, v_{\parallel})$ ,  $\Delta t$  is the time interval and  $\delta\phi^{(i)}$  is solved from Eq. 33 with  $\delta n(t)$  obtained using  $\mathbf{X}_t^{(i)}$  for  $i = 1, 2, 3$ .

### 2. Particle positioning (deposition) scheme

When calculating the toroidal component of the density perturbation  $\delta n_n(R, Z)$  in Eq. 32 using marker weight  $w_p$  in the so-called ‘‘deposition’’ stage, the marker-triangle mapping, i.e., the particle positioning, needs to be treated. For the brute force particle position scheme, each triangle is checked for each marker whether the triangle contains the marker, which leads to  $NN_t$  computational cost, where  $N$  and  $N_t$  are marker and triangle numbers respectively. In this work, rectangular grids (‘‘boxes’’) are constructed in  $(R, Z)$  space and the box-triangle index  $\text{Box}_i \mapsto \text{Triangle}_j$  is built when there is overlap between a box  $i$  and a triangle  $j$ . The mapping

$\text{Box}_i \mapsto \text{Triangle}_j$ ,  $j = 1, \dots, N_{i,\text{tri}}$  is stored in the dynamically growing arrays for each box  $i$ . For a given marker  $p$ , the box which contains Marker  $p$  is first found, i.e., the  $p \mapsto \text{Box}_i$  is found. Then using the box-triangle mapping  $\text{Box}_i \mapsto \text{Triangle}_j$ , the corresponding triangle is identified. The computational cost is  $\alpha N$  for  $N$  markers, where  $\alpha$  is a constant number.

The intermediate box is generated in the simulation domain with  $N_x$  and  $N_y$  specified, where  $N_x$  and  $N_y$  are the rectangular grid numbers in  $R$  and  $Z$  directions. One limit is  $N_x \ll N_r$ , where  $N_r$  is the radial grid number of the unstructured meshes. For  $N_x = 2$  (the box number is one), the positioning scheme is identical to the brute force scheme. The other limit is  $N_x \gg N_r$ , for which the box size is much smaller than the triangle size. The typical case among these two limit cases is that with  $N_x \approx N_r$ . These three cases are shown in Fig. 2. The computational cost versus the box size or  $N_x$  will be studied in Sec. III.

## III. NUMERICAL RESULTS

### A. Parameters and simplifications for the simulation

In this section, two experimental cases are discussed. For numerical studies and benchmarks in Sections IIIB and IIIC, the DIII-D Cyclone case is adopted, for which the parameters are the same as those in the benchmark work<sup>26</sup>. A circular concentric magnetic equilibrium is assumed. The safety factor profile in the previous benchmark studies<sup>26</sup> is

$$q(r) = 2.52\bar{r}^2 - 0.16\bar{r} + 0.86 , \quad (37)$$

where  $\bar{r} \equiv r/a$ . In Sections IIIB and IIIC, an Ad-hoc equilibrium model is adopted. By assuming the following form of the safety factor profile,

$$q(r) = q_0 + q_2\bar{r}^2 , \quad (38)$$

the poloidal flux function can be obtained analytically<sup>21,27</sup>. The values of  $q$  and the magnetic shear  $\hat{s}$  are matched to Eq. 37 at  $r_c = 0.5a$ , i.e.,  $q_2 = q_c \hat{s}_c / (2r_c^2)$ ,  $q_0 = (2/\hat{s}_c - 1)\bar{r}_c^2 q_2$ , where  $q_c$  and  $\hat{s}_c$  are calculated at  $r = r_c$  using Eq. 37. The temperature and density profiles indicated by  $A(r)$  and the corresponding normalized logarithmic gradients indicated by  $L_{ref}/L_A$  are given by

$$\frac{A(r)}{A(r_0)} = \exp \left\{ -\kappa_A W_A \frac{a}{L_{ref}} \tanh \left( \frac{r - r_c}{W_A a} \right) \right\} , \quad (39)$$

$$\frac{L_{ref}}{L_A} = -L_{ref} \frac{d \ln A}{dr} = \kappa_A \cosh^{-2} \left( \frac{r - r_c}{W_A a} \right) , \quad (40)$$

where the subscript ‘c’ denotes the center of the gradient and the values of  $r_c$ ,  $W_A$  etc are in Table I.

For the studies using the realistic geometry in Section IIID, the ASDEX Upgrade (AUG) case with shot number 034924 at 3.600s is chosen. This is a typical discharge

$r_c/a$	$a/R_0$	$a/\rho_s$	$T_e/T_i$	$R_0/L_{ref}$	$\kappa_{Ti}$	$\kappa_n$	$W_n = W_{Ti}$
0.5	0.36	180	1	1	6.69	2.23	0.3

TABLE I. Parameters for ITG with adiabatic electrons (same as those in Ref. 26), where  $R_0 = 1.67m$ ,  $\rho_s = c_s/\Omega_i$ ,  $c_s = \sqrt{T_e/m_i}$  and the value of  $\rho_s$  is calculated using  $T_e(r/a = 0.5)$  and  $B(r = 0)$ .

for the study of the energetic particle and turbulence physics<sup>28</sup>. In the simulation, we use the experimental equilibrium but use the analytical density and temperature profiles in Eq. 40, with the radial coordinate replaced with  $\rho_p = \sqrt{(\psi - \psi_0)/(\psi_b - \psi_0)}$ , where  $\psi_0$  and  $\psi_b$  are the poloidal magnetic flux function at the magnetic axis and the boundary respectively. The purpose of this study is to test the capability of treating the realistic geometry. The fully self consistent treatment of the density/temperature profile and the equilibrium will be addressed in another work.

Since our purpose is to study the mixed PIC-PIF scheme and the particle position scheme in this work and address the basic ITG mode problem in the whole device geometry with minimum complexity, we have made the following simplifications.

1. The dominant terms in the equations of motion, Eqs. 17, 21 and 23, are solved.
2. The equilibrium variation of  $n$ ,  $B$  and  $T$  in the Poisson equation, Eq. 33, is ignored.
3. The ITG instability drive in Eq. 40 for the weight equation is kept but the equilibrium variation in  $n$ ,  $T$  and  $B$  is omitted.
4. A single toroidal harmonic is simulated without the nonlinear term, even though the dominant nonlinear term  $\delta v_E \cdot \nabla \delta f$  for the ITG saturation is implemented in TRIMEG.

This simplified model can be replaced with a more comprehensive one by either future development of the TRIMEG code, or by implementing the finite element solver for unstructured meshes and PIC-PIF solver in other codes such as ORB5 and GTC.

## B. Convergence and scaling studies

The effects of the rectangular box size on the computational cost in the particle positioning scheme is studied using a medium size case whose radial grid number is  $N_r = 90$  and the total marker number is 25.6 millions. The brute force scheme ( $N_x = 2$ ) serves as the baseline and the speed-up for other values of  $N_x = N_y = 4, 8, \dots, 4096, 8192$  are shown in Fig. 3. There is an optimal value of the box size with respect to the triangle size in the range of  $1 < N_x/(2N_r) < 10$ . The speed-up

for  $N_x = 256, 512, 1024$  are 35.5, 35.7, 36.3, larger than that for other  $N_x$ . For  $N_x/(2N_r) \ll 1$ , each box contains a large number of triangles, as shown in Fig. 2 (left) and identifying the particle-triangle mapping consumes significant calculations. For  $N_x/(2N_r) \gg 1$ , the memory cost for storing the box-triangle mapping increases but without significant CPU cost, and thus only slows down the simulation slightly. Even as  $N_x$  changes from 1024 to 8192, the speed-up changes from 36.3 to 32.7, only around 10%.

The convergence of the simulation results in terms of growth rate with respect to the radial grid number, the marker number per triangle and the time step size is studied. The convergence with respect to  $N_r$ , marker number  $N$  and time step size  $\Delta t$  is shown in Fig. 4. For this  $n = 20$  mode, as shown in the left frame, from  $N_r = 64$ , the simulation starts to converge. The corresponding poloidal grid number per wave length  $\approx 7$ . Note that the poloidal grid size is set to be close to the radial grid size. For the linear studies in this work, the mode structure is elongated along the radial direction and the low limit of  $N_r$  is determined by the grid number per wave length in poloidal direction, i.e.,  $N_\theta/m \approx 2\pi N_r(r/a)/(nq) \gg 1$ . In the middle frame, the results start to converge when the marker number per triangle  $N/N_t > 4$ . In the right frame, the simulation starts to converge for  $dt \leq 0.5$  and become numerically unstable for  $dt > 1$ .

The parallel performance is tested for evaluating the scaling properties. The speed-up for the simulation with  $N = 25.6$  millions markers with different values of the core number is analyzed and shown in Fig. 5. Its comparison with the ideal scaling shows the good strong scaling for small to moderate core numbers (core number  $\leq 1280$ ). For even larger core numbers, the consumption of the field solver parallel communication can increase since the field solver is distributed over all cores. As a result, the deviation of the speed-up curve away from the ideal scaling becomes significant as the core number is larger than 1280.

## C. ITG simulation using Cyclone parameters

Following the convergence and scaling studies in Section III B, ITG mode simulations using the Cyclone case parameters are performed. The growth rate and the frequency are shown in Fig. 6 and are converted to compare with the ORB5 results noticing  $v_{ti}/R_N = \sqrt{2T_i/T_e}(R_0/R_N)(c_s/R_0)$ , where  $R_0$  is the major radius. The agreement between the TRIMEG results and the ORB5 results is reasonable, noticing the simplification in TRIMEG as discussed in Sec. III A. Nevertheless, considering the spatial scale separation between the equilibrium profile variation spatial scale  $L_E$ , the mode structure radial envelop width  $L_A$  and the single poloidal harmonic width  $1/(ndq/dr)$ , i.e.,  $L_E \gg L_A \gg 1/(ndq/dr)$ <sup>29</sup>, the simulation from TRIMEG already captures the leading order solution. More comprehensive physics models will

Case	OFL	$\rho_{p,c}$	$W_{p,c}$
A	w/o	0.5	0.3
B	w/	0.5	0.3
C	w/	1.0	0.1

TABLE II. Parameters for the three ITG simulations using the AUG equilibrium. OFL refers to Open Field Line. For all cases,  $\kappa_n = 2.23$ ,  $\kappa_T = 6.96$ .

be implemented in future.

#### D. ITG simulation using AUG equilibrium in the core plasma and in the whole device geometry

In this section, we perform the simulation of an ITG mode using the AUG equilibrium described in Section III A. The main purpose is to demonstrate the capability of treating the realistic magnetic equilibrium from an experiment using TRIMEG. Three cases are defined in Table II. The simulation without and with the open field line region are performed and compared as shown in Fig. 7 and Fig. 8. For Cases (A) and (B), the open field line plays a weak role on the core ITG mode due to the narrow envelope of the radial mode structure. As a result, the 2D mode structures and the growth rate are almost identical between these two cases. For Case C, the local variables at  $\psi = \psi_b$  such as  $q$ ,  $\hat{s}$ , and the minor radius that determine the mode growth rate are different from (A) and (B). As a result, the growth rate curve is shifted due to the change in the finite Larmor radius / finite orbit width effects ( $k_\theta \rho_{th} \approx nq \rho_{th} / r$ ) and other effects. While the convergence of the simulation for the whole plasma volume is achieved, a benchmark with other codes with the treatment of the whole device geometry will be studied in future. More comprehensive models for the edge physics also need to be considered<sup>12,13</sup>.

#### IV. CONCLUSION

In this work, the TRIMEG code has been developed based on the mixed unstructured mesh based FEM-Fourier decomposition scheme and the intermediate grids for particle deposition. The parallel scalability of particle deposition has been achieved and strong scaling up to moderate core numbers has been demonstrated. The benchmark with ORB5 using the DIII-D Cyclone test case shows reasonable agreement in terms of growth rate and frequency. The capability of treating the whole plasma volume is demonstrated by using an AUG magnetic equilibrium with X-point and analytical density and temperature profiles. Further development of the TRIMEG code for more comprehensive simulations including wave-particle, wave-wave nonlinearity and multiple species will be explored in future.

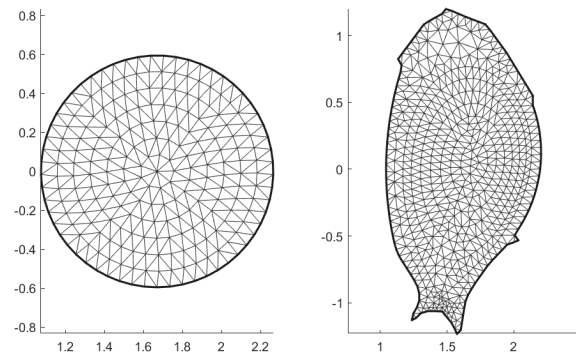


FIG. 1. The grids and meshes for the Cylone case and the AUG case used in Section III. The grids shown in the figure are much sparser than those used in simulations.

#### ACKNOWLEDGMENT

Simulations were performed on MPCDF computing systems. Suggestions from ORB5, EUTERPE, MHGC, GTC and GTS groups, discussion with B.D. Scott, D. Coster, A. Bierwage and support by National Natural Science Foundation of China under Grant No. 11605186 are appreciated by ZL. ZL thanks X. Wang for naming the code with TRIMEG. Support by the ENR projects “NAT” and “MET” is acknowledged. This work has been carried out within the framework of the EUROfusion Consortium and has received funding from the Euratom research and training programme 2014-2018 and 2019-2020 under grant agreement No 633053. The views and opinions expressed herein do not necessarily reflect those of the European Commission.

- <sup>1</sup>WW Lee. *Phys. Fluids*, 26(2):556, 1983.
- <sup>2</sup>Z Lin, WM Tang, and WW Lee. *Phys. Plasmas*, 2(8):2975, 1995.
- <sup>3</sup>Z Lin, TS Hahm, WW Lee, WM Tang, and RB White. *Science*, 281(5384):1835, 1998.
- <sup>4</sup>WX Wang, S Ethier, Y Ren, S Kaye, J Chen, E Startsev, and Z Lu. *Nucl. Fusion*, 55(12):122001, 2015.
- <sup>5</sup>S Ku, Choong-Seock Chang, and PH Diamond. *Nucl. Fusion*, 49(11):115021, 2009.
- <sup>6</sup>F Jenko, W Dorland, M Kotschenreuther, and BN Rogers. *Phys. Plasmas*, 7(5):1904, 2000.
- <sup>7</sup>W Dorland, F Jenko, Mike Kotschenreuther, and BN Rogers. Electron temperature gradient turbulence. *Phys. Rev. Lett.*, 85(26):5579, 2000.
- <sup>8</sup>SE Parker, Y Chen, and CC Kim. *Comput. Phys. Commun.*, 127(1):59–70, 2000.
- <sup>9</sup>S Jolliet, A Bottino, P Angelino, R Hatzky, TM Tran, BF Mcmillan, O Sauter, K Appert, Y Idomura, and L Villard. *Comput. Phys. Commun.*, 177(5):409, 2007.
- <sup>10</sup>CS Chang, S Ku, A Loarte, V Parail, F Koechl, M Romanelli, R Maingi, JW Ahn, T Gray, J Hughes, et al. *Nucl. Fusion*, 57(11):116023, 2017.
- <sup>11</sup>GTA Huysmans and O Czarny. *Nucl. Fusion*, 47(7):659, 2007.
- <sup>12</sup>H Qin, RH Cohen, WM Nevins, and XQ Xu. *Contrib. Plasma Phys.*, 46(7):477, 2006.
- <sup>13</sup>BD Scott. *Contrib. Plasma Phys.*, 46(7):714, 2006.

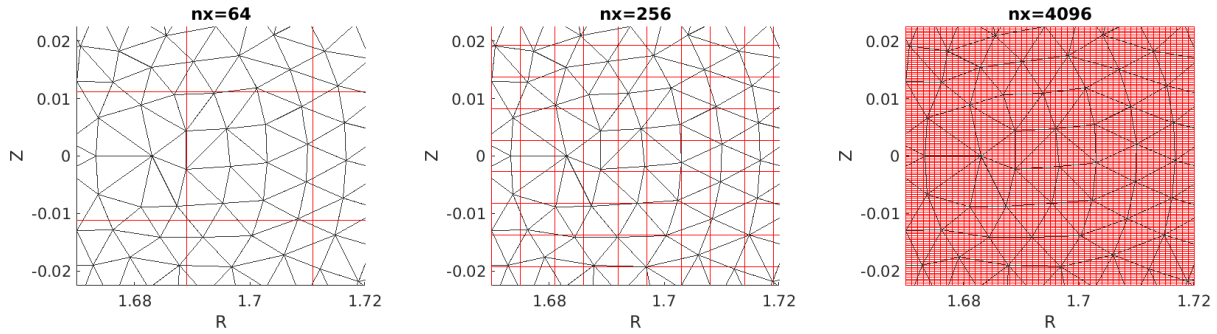


FIG. 2. The box (red lines) size and its comparison with the triangle (black lines) size for different values of  $N_x$ . Cyclone parameters are used and the radial grid number  $N_r = 90$ .

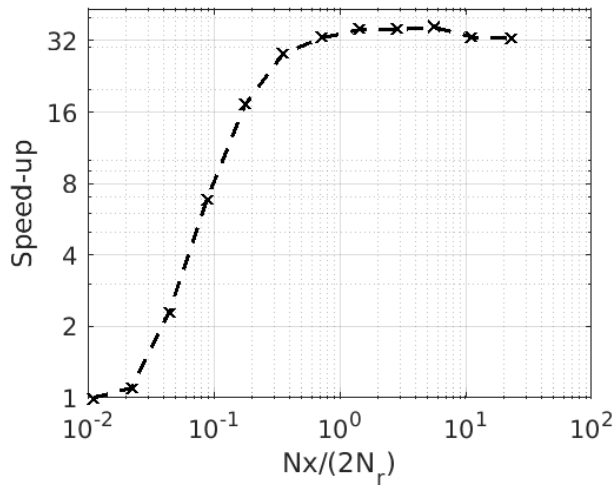


FIG. 3. The speed-up of a medium size simulation ( $N_r = 90$ , 25.6 million markers) for different values of  $N_x/(2N_r)$ .

- <sup>14</sup>NM Ferraro, Stephen C Jardin, and PB Snyder. *Phys. Plasmas*, 17(10):102508, 2010.
- <sup>15</sup>Y Nishimura, Z Lin, JLV Lewandowski, and S Ethier. *J. Comput. Phys.*, 214(2):657, 2006.
- <sup>16</sup>J Bao, CK Lau, Z Lin, HY Wang, DP Fulton, S Dettrick, and T Tajima. *Phys. Plasmas*, 26(4):042506, 2019.
- <sup>17</sup>S De, T Singh, A Kuley, J Bao, Z Lin, GY Sun, S Sharma, and A Sen. *arXiv preprint arXiv:1702.04075*, 2017.

- <sup>18</sup>D. C. van Vugt, G. T. A. Huijsmans, M. Hoelzl, and A. Loarte. *Phys. Plasmas*, 26(4):042508, 2019.
- <sup>19</sup>J Ameres. *Stochastic and Spectral Particle Methods for Plasma Physics*. PhD thesis, Technische Universität München, 2018.
- <sup>20</sup>N Ohana, A Jocksch, E Lanti, AL Scheinberg, S Brunner, C Gheller, and L Villard. In *17th European Fusion Theory Conference*, 2017.
- <sup>21</sup>ZX Lu, Ph Lauber, X Wang, A Bottino, A Mishchenko, and J Chen. The mixed unstructured fem-fourier decomposition scheme as a fast linear solver for studies of tokamak plasma waves and instabilities. *to be submitted*, 2019.
- <sup>22</sup>JR Shewchuk. *Computational geometry*, 22(1):21, 2002.
- <sup>23</sup>RB White. *Phys. Fluids B*, 2(4):845, 1990.
- <sup>24</sup>E Lanti, N Ohana, N Tronko, T Hayward-Schneider, A Bottino, BF McMillan, A Mishchenko, A Scheinberg, A Biancalani, and P Angelino et al. Orb5: a global electromagnetic gyrokinetic code using the pic approach in toroidal geometry. *submitted*, 2019.
- <sup>25</sup>S Balay, S Abhyankar, M Adams, J Brown, P Brune, K Buschelman, L Dalcin, A Dener, V Eijkhout, W Gropp, et al. *Petsc users manual*. 2019.
- <sup>26</sup>T Görler, N Tronko, WA Hornsby, A Bottino, R Kleiber, C Norscini, V Grandgirard, F Jenko, and E Sonnendrücker. *Phys. Plasmas*, 23(7):072503, 2016.
- <sup>27</sup>A Bottino, AG Peeters, R Hatzky, S Jolliet, BF McMillan, TM Tran, and L Villard. *Phys. Plasmas*, 14(1):010701, 2007.
- <sup>28</sup>P Lauber, B Geiger, G Papp, GI Pokol, A Biancalani, X Wang, Z Lu, P Pölöskei, A Bottino, F Palermo, et al. Strongly nonlinear energetic particle dynamics in asdex upgrade scenarios with core impurity accumulation. In *27th IAEA Fusion Energy Conference (FEC 2018)*, 2018.
- <sup>29</sup>ZX Lu, F Zonca, and A Cardinali. *Phys. Plasmas*, 19(4):042104, 2012.
- <sup>30</sup>ZX Lu, E Fable, WA Hornsby, C Angioni, A Bottino, Ph Lauber, and F Zonca. *Phys. Plasmas*, 24(4):042502, 2017.

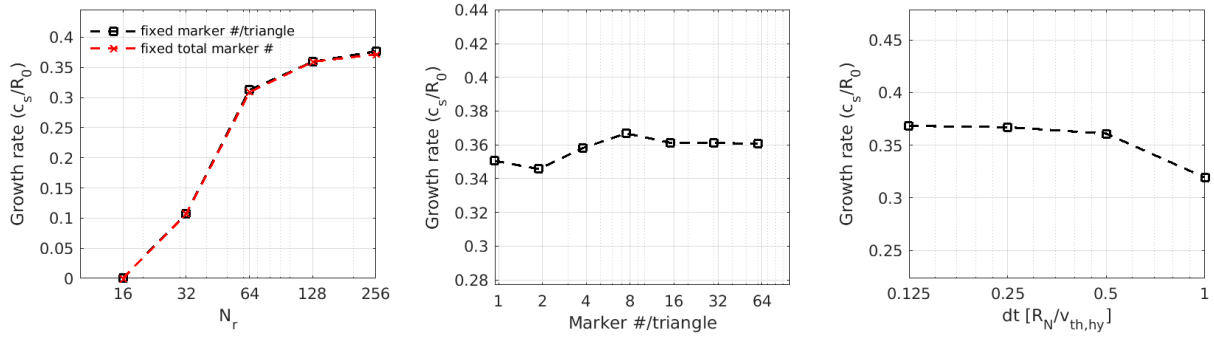


FIG. 4. The convergence study for the growth rate of the ITG instability with respect to the grid number (left), marker number (middle) and time interval (right). The parameters for the base are  $n = 20$ ,  $N_r = 128$ , 15 markers per triangle,  $dt = 0.5$  and the scans are performed from the base case. In the left frame, the black line corresponds to the scan with 15 markers per triangle fixed. The red line with squares corresponds to the scan with 1.6 million markers fixed (15 markers per triangle for  $N_r = 128$ ).

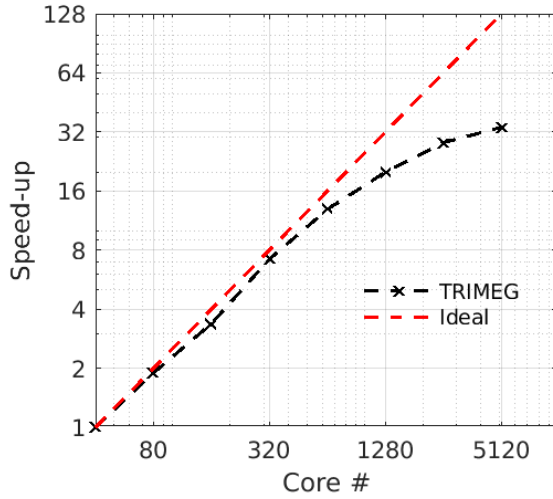


FIG. 5. The speed-up of the simulation versus the core number in TRIMEG simulation (black dashed line with crosses) and its comparison with the ideal scaling (red dashed line).

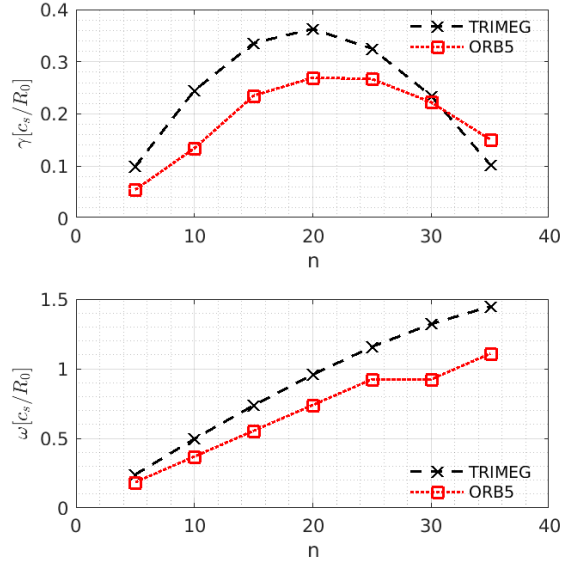


FIG. 6. Benchmark of the growth rate (upper) and the real frequency (bottom) for the Cyclone case. The ORB5 simulation results are from our previous work<sup>30</sup>.

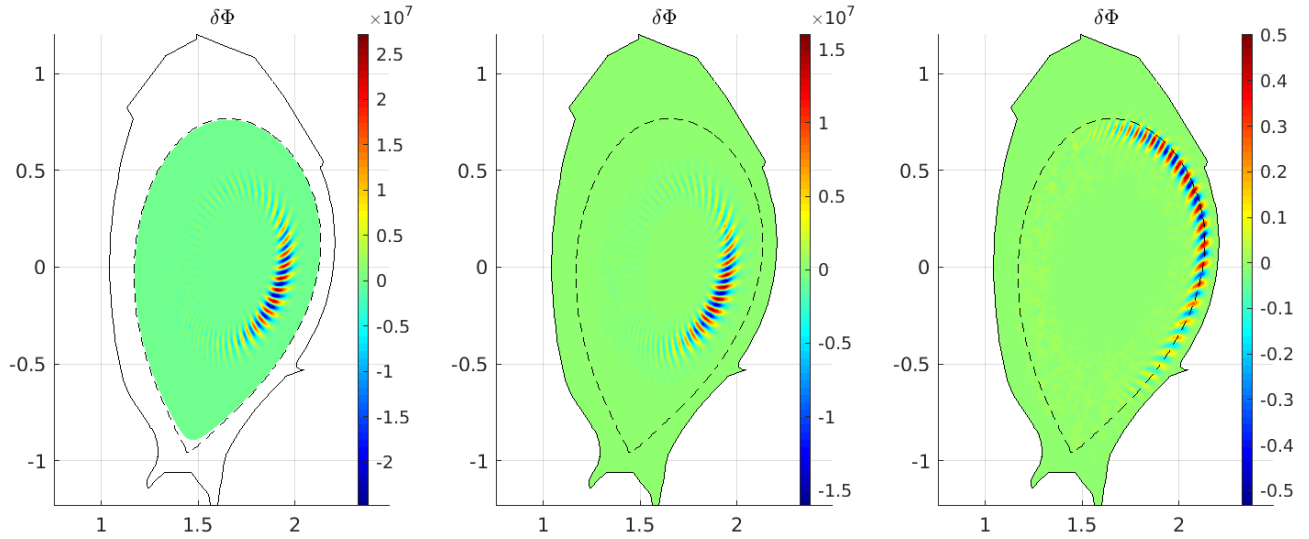


FIG. 7. The 2D ITG mode structures ( $n = 20$ ) for the three cases defined in Table II. Case A (left), Case B (middle) and Case C (right). The dotted line indicates the separatrix.

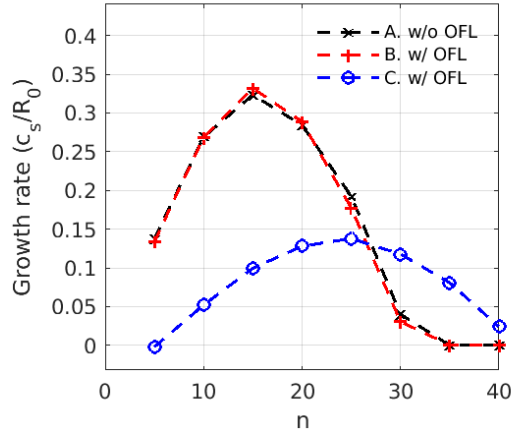


FIG. 8. Growth rate versus toroidal mode number  $n$  for the three cases defined in Table II.